ACS APPLIED MATERIALS & INTERFACES

Research Article

Cite This: ACS Appl. Mater. Interfaces 2019, 11, 2273−2281

www.acsami.org

Symmetry Breaking-Induced Plasmonic Mode Splitting in Coupled Gold−Silver Alloy Nanodisk Array for Ultrasensitive RGB Colorimetric Biosensing

Ibrahim Misbah,[†] Fusheng Zhao,[†] and Wei-Chuan Shih*[,†,‡,§,∥]

[†]Department of Electrical and Computer Engineering, [‡]Department of Biomedical Engineering, [§]Program of Materials Science and Engineering, and [∥]Department of Chemistry, University of Houston, 4800 Calhoun Road, Houston, Texas 77204, United States

Supporting Information

ABSTRACT: We report the first observation of symmetry breaking-induced mode splitting in coupled gold−silver alloy nanodisk array (ANA). According to the plasmonic hybridization picture, the original localized surface plasmon resonance (LSPR) of individual nanodisk is split into a pair of high and low energy modes when placed in between a superstrate and a substrate. Although well studied in single silver nanoparticles, the high energy mode has been largely suppressed in gold nanoparticles, which nevertheless are more chemically robust and have superior environmental stability. Herein, we show that the high energy mode can be partially restored and precisely engineered to ∼540 nm for silver-rich alloy nanodisk which has excellent environmental stability. However, peak broadening and red-shifting occur due to plasmonic dephasing when the nanodisk diameter increases. We next demonstrate that a far-field coupled ANA fabricated by low-cost nanosphere lithography can fully restore the high energy mode with electric field concentration extended into the superstrate, thereby imparting greater sensitivity to local refractive index changes. The high energy mode at 540 nm is of key importance for color change detection using low-cost RGB cameras/human vision and broadband light sources (e.g., the sun). The index sensitivity of ANA is the highest among existing plasmonic arrays (particles or holes) within a similar resonance wavelength region. We demonstrate colorimetric detection of sub-nanomolar and sub-monolayer biotin−streptavidin surface binding with a smartphone camera and a white light lamp. The high performance yet low-cost fabrication and detection technology could potentially result in affordable point-of-care biosensing technologies.

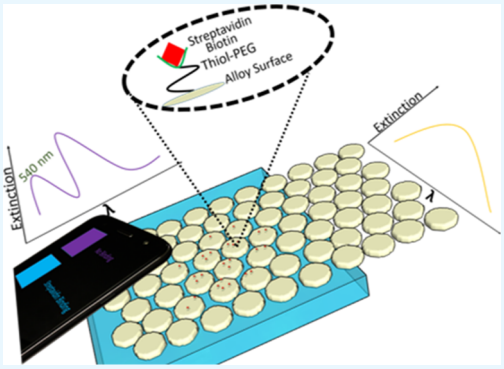

KEYWORDS: *plasmonic nanoparticles array, plasmonic hybridization and mode splitting, gold-silver alloy nanodisk array, smartphone colorimetric detection, plasmonic biosensing*

INTRODUCTION

Metal nanoparticles possess fascinating optical properties due to light-induced collective oscillation of conduction band electrons, a phenomenon known as localized surface plasmon resonance (LSPR).[1,2] LSPR has been the basis for various applications in sensing,[3] imaging,[4] energy conversion,[5] and catalysis.[6] The specific LSPR frequency and bandwidth typically depend on the material, shape, size, and the surrounding dielectric medium of the nanoparticles.[7−9] In particular, recent advances in nanofabrication and synthesis allow for the fine-tuning of the LSPR properties over a broad spectral range. Significant efforts have been placed to understand the plasmonic interactions of nanoparticle "ensembles" from a group of isolated nanoparticles.[10,11] Such plasmonic interactions of the constitutional nanoparticles lead to the modification and generation of new resonances.[11,12] These interactions are also range-dependent and can be classified as near-field and far-field interactions. Plasmonic hybridization theory can provide explanations analogous to the molecular orbital theory.[13]

According to the plasmonic hybridization theory, when two nanoparticles are placed in close proximity to each other, the interaction leads to the hybridization of the individual plasmon modes and results in bonding and antibonding modes with their properties dictated by the interaction mechanism.[13] The theory of plasmonic hybridization has been extensively applied to study nanoparticles interactions like nanoparticle dimers,[14] spherical nanoparticles,[15] and nanoparticle crescents.[16] Moreover, the approach also explains complex nanoparticle interaction like nanoparticles sitting on a metallic or a dielectric substrate.[17,18] A key scenario in the plasmonic hybridization theory is symmetry breaking, which can be modeled by placing the nanoparticle on an interface met by a substrate and a superstrate.

Sherry et al. studied the symmetry breaking in a single silver nanocube by changing its distance to a glass substrate.[19] As the

Received: October 12, 2018
Accepted: December 20, 2018
Published: December 20, 2018

DOI: 10.1021/acsami.8b17876
ACS Appl. Mater. Interfaces 2019, 11, 2273−2281

silver nanoparticle approaches the glass substrate, mode splitting was observed and subsequently verified using finite difference time domain (FDTD) simulations. Ringe et al. further elucidated that the symmetry breaking also caused uneven electric field (E-field) localization: the E-field associated with the higher energy LSPR peak concentrated toward the lower index dielectric medium (i.e., air superstrate), whereas the E-field of the lower energy LSPR peak concentrated toward the higher index dielectric medium (i.e., glass substrate).[20] Zhang et al. attributed the mode splitting to coupling and hybridization using plasmonic hybridization theory.[21] They further interpreted this phenomenon as a Fano-resonance, which arises from the interference between two spectrally overlapping broad and narrow resonances. The hybridized higher energy peak in these articles has narrower linewidth measured by full-width-at-half-maximum. Similar to the dipolar LSPR common in all nanoparticles, the hybridized modes are also sensitive to the refractive index (RI) of the surrounding medium. More importantly, the higher energy peak has higher RI sensitivity compared to the lower energy peak presumably due to their differences in E-field distribution. This finding was very interesting because lower energy LSPRs typically have higher RI sensitivity[22] and can have profound implication to engineering high RI sensitivity in the visible wavelength.

The LSPR-induced evanescent field makes metal nanoparticles highly sensitive to absorption and binding of specific molecules onto their surface, enabling label-free sensing and quantification by colorimetric analysis.[2,23,24] As a rule of thumb, the LSPR sensitivity (i.e., the amount of peak shift induced by a unit change of RI, having the units of nm/RIU) scales with the LSPR peak position in air.[25] Therefore, most of the sensitive plasmonic sensors reported in the literature have LSPR peak in the red or near-infrared (NIR) region.[26,27] With such sensors, the red shift in the plasmonic peak due to surface binding do not induce a substantial color change in the visible wavelength range. For example, sensors based on extraordinary optical transmission (EOT) around 700 nm required a spectrally aligned LED light source with a bandwidth less than 50 nm. The peak shift in the EOT sensor was then detected as reduced light transmission. Such a scheme required highly accurate intensity measurements and relied on sophisticated fabrication processes to generate a sharp resonance.[28] Another category of techniques relies on controlled aggregation of colloidal nanoparticles suspension, which can induce stronger peak shift and color change than surface modification.[29−31] However, undesirable aggregation and shelf life are always significant concerns in colloidal nanoparticle-based approaches.[32]

Although the higher energy peak is more sensitive, its wide application has been limited because silver is chemically reactive and is generally unstable in the environment. Unfortunately, the high energy peak has not been observed in more chemically stable gold nanostructures as the resonance occurs near the interband transition region for gold. In this article, we show that we can fully harvest the potential of this high energy peak from disk-shaped alloy nanoparticles in a high-density, plasmonically coupled array. Instead of using gold or silver as the only material which has their advantages and disadvantages discussed above, gold−silver alloy in the ratio of 30:70 has been adopted. The gold−silver alloy is significantly more chemically stable than silver alone while sustaining the higher energy peak much better than gold alone. Finally, the high-density array introduces strong far-field plasmonic coupling (FFPC), which boosts the otherwise insignificant higher energy mode for large size disks (350 nm in diameter, 80 nm in thickness).

This novel plasmonic substrate can be of significant and broad interest in developing biosensing techniques due to limited resources or cost concerns.[32−34] By utilizing the high energy mode, low-cost RGB cameras such as those found on smartphones can be employed for colorimetric readout, which is otherwise not feasible when the LSPR does not reside in the green wavelength range. Smartphones as imaging sensors have been widely utilized in resource-limited settings because of their portability, affordability, high-quality camera, wireless communication, and computational capability.[35−37] Smartphones have been employed for colorimetric detection as well as microscopic imaging.[35,38] Various colorimetric techniques such as enzyme-linked immunosorbent assay, lateral flow immunoassays, and redox reaction-related chemiluminescence are paired with a smartphone for improved color quantification.[39−41]

In this work, by taking advantage of the large tuning range of the plasmonic resonance of gold−silver alloy disks in an array, we have designed a substrate so that the higher energy peak is located at ∼540 nm, the most sensitive region for RGB cameras. Combined with high RI sensitivity, we demonstrate the detection of minute protein−protein conjugation using a smartphone camera, suggesting a highly versatile platform for point-of-care biosensing applications.

RESULTS AND DISCUSSION

Alloy nanodisk arrays (ANAs) were fabricated by nanosphere lithography (NSL) using 460 nm polystyrene (PS) beads with the alloy consisting of 30% gold and 70% silver in the atomic ratio. The lattice constants in the ordered regions are equal to the starting PS bead size of 460 nm. The ANAs have a thickness of 80 nm and diameters of 350 nm. The exact size of the nanodisks is controlled by the shrinkage time of the PS beads during oxygen plasma etching. Typical SEM images of ANA fabricated with 460 nm PS beads are shown in Figure 1. The arrays possess "polycrystalline" characteristics, where the

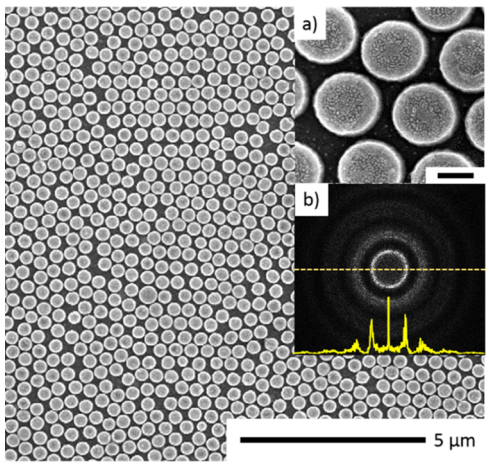

Figure 1. Typical SEM images of samples fabricated using 460 nm PS beads, showing a polycrystalline structure. Inset (a): Zoomed in SEM image, the scale bar is 200 nm. Inset (b): FT image of the SEM image, the ring-shaped pattern further verifies the overall disorderliness.

DOI: 10.1021/acsami.8b17876
ACS Appl. Mater. Interfaces 2019, 11, 2273−2281

PS beads are closely packed into hexagonal arrays in domains with a characteristic size around microns to tens of microns.

Figure 2 shows both the measured and simulated extinction spectra of the ANA array in air (black line) and water (red line). It is known that the deviation from perfectly periodic arrangement causes noticeable but insignificant peak broadening and peak intensity decrease.[11] The alloy dielectric function was calculated using values found in ref 42. The higher energy peak appearing around ~540 nm has a smaller width, whereas the lower energy peak around ~750 nm is much broader. Unless otherwise stated, the higher energy peak and the lower energy peak will be called P1 and P2, respectively. As shown in Figure 2, both peaks undergo a red shift by changing the surrounding medium from air to water. However, the amount of red shift is much more substantial for P1. In water, we also observe the appearance of another peak owing to the presence of more hybridized peaks in the higher RI environment. The same reasoning is applicable for the nanodisks with larger sizes and pitches. All of their extinction responses result from the combination of hybridized bonding/antibonding modes of individual nanoparticles because of the symmetry breaking. This symmetry breaking is coming from both the neighboring nanoparticles in the vicinity and the presence of glass substrate.

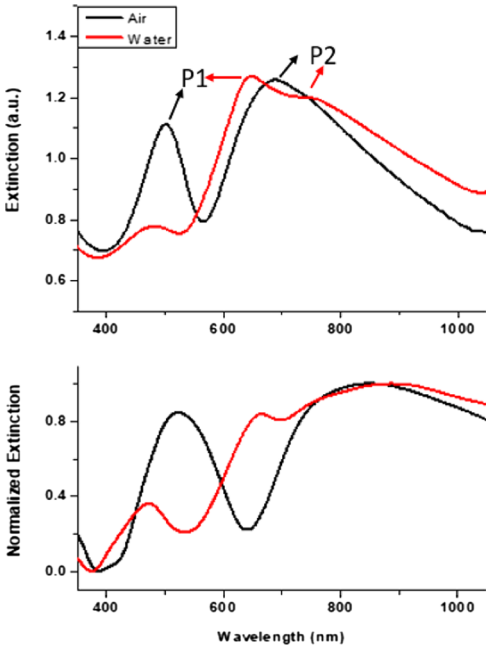

Figure 2. Experimentally measured extinction spectra (top) and FDTD simulated extinction spectra (bottom) of samples fabricated with 350 nm disk diameter with 460 nm mean lattice constant. Spectra in air (black line) and water (red line) were measured and calculated.

A FDTD simulation was set up to investigate the physical origin of these hybridized modes, P1 in particular, where the separation distance between the ANA and the substrate was varied from infinity to 0. The ANA consisted of 100 nanoparticles in a 10 × 10 array in a semi-random hexagonal pattern, resembling the configuration obtained by NSL. The RI of the substrate and superstrate was 1.52 and 1, respectively. As shown in Figure 3a, when the separation distance was infinity, only one broad peak (P2) was observed. As the separation distance decreased, the high energy peak (P1) emerged. Eventually, clearly separated P1 and P2 were observed as in the previous experiment as the ANA came in contact with the substrate.

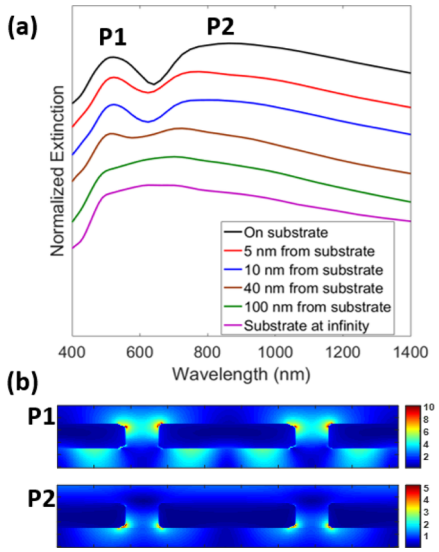

Figure 3. (a) Emergence of separated P1 and P2 peaks as the ANA is brought into contact with the glass substrate from infinity. (b) E-field distribution for wavelengths corresponding to P1 and P2 when the ANA is in contact with the glass substrate.

Figure 3b shows the E-field distribution near individual disks in the ANA when they are in contact with the substrate. It is observed that P1 has an E-field profile that concentrates mostly at the upper corners where the surrounding medium is the superstrate. In contrast, the E-field distribution for P2 concentrates primarily at the lower corners with a significant portion inside the substrate. These simulation results are consistent with those for single silver nanocubes published by Sherry et al.[19]

To experimentally prove that the mode splitting was indeed due to symmetry breaking by introduction of the substrate, we have immersed the ANA sample in index-matching fluid with RI = 1.52. The experimental results shown in Figure 4 indicates the disappearance of P1 and the restoration of the

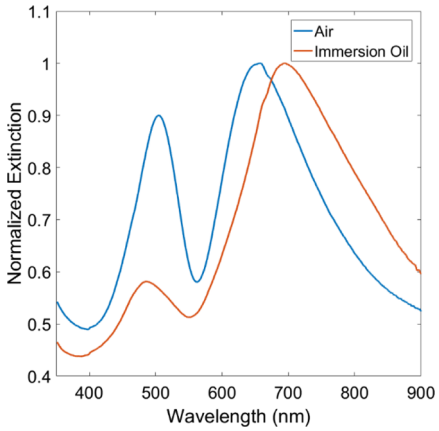

Figure 4. Experimentally measured extinction spectra of samples fabricated with 350 nm disk diameter with 460 nm mean lattice constant. Spectra in air (blue line) and immersion oil having RI of 1.52 (red line) are displayed.

DOI: 10.1021/acsami.8b17876
ACS Appl. Mater. Interfaces 2019, 11, 2273−2281

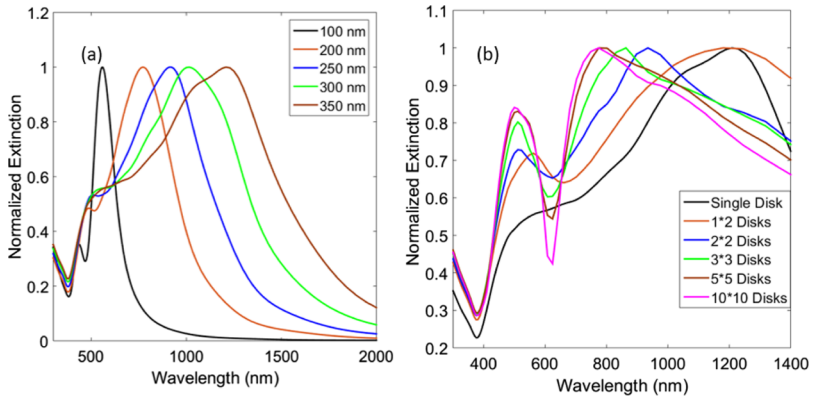

Figure 5. (a) Simulated extinction spectra of a single alloy nanodisk with different diameters. (b) Effect of array size varying from a single disk to a 10 × 10 array. The disk diameter was 350 nm with 460 nm mean lattice constant.

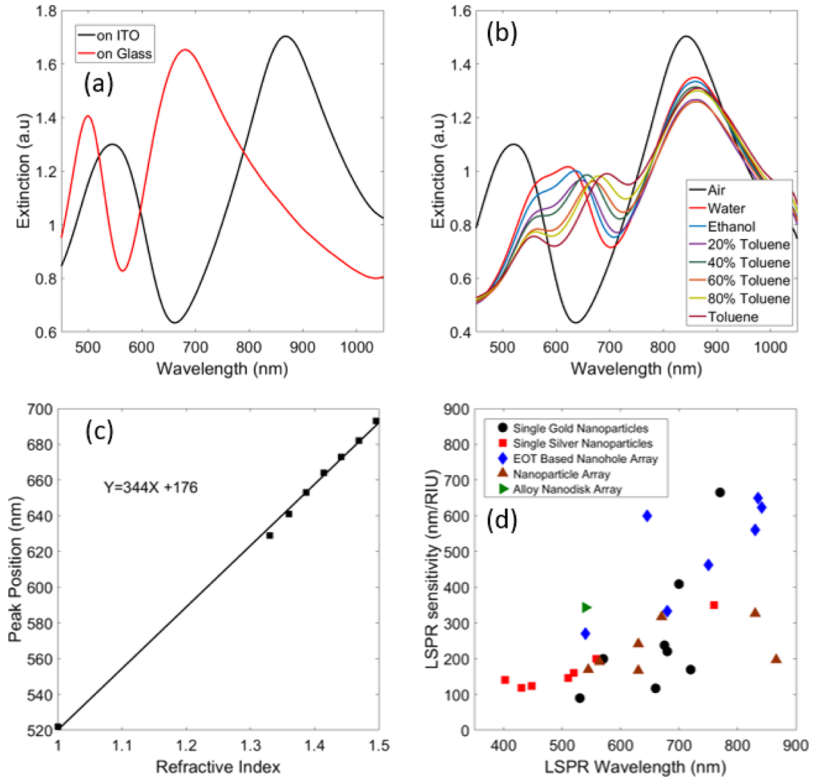

Figure 6. (a) Extinction spectra of alloy disk arrays with a lattice constant of 460 nm fabricated on glass (red) and ITO-coated glass (black) substrate. (b) Extinction spectra of alloy disk on ITO substrate in different surrounding media. (c) LSPR position of peak P1 plotted against the RI. (d) Comparison of RI sensitivity of representative plasmonic nanostructures with ANAs.

original LSPR without symmetry breaking. Another peak which has even higher energy than P1 is observed in both the experimental and simulation results and can be assigned to higher hybridized mode among neighboring disks in the higher RI scenario. We note that this peak was present but largely buried in the previous simulation results (Figure 3a).

Next, we discuss the choice of ANA consisting of disks with 350 nm diameter and 80 nm thickness. To investigate the size and array effects, we have conducted a series of simulations with various disk diameters and array sizes. First, we studied the diameter dependence of a single alloy disk. As shown in Figure 5a, a single 100 nm diameter alloy disk on glass substrate has both P1 and P2 (black curve) with P1 in the blue color region. To engineer P1 into the green color region, the disk diameter was increased from 100 to 350 nm. Although both peaks red-shift, they also suffer significant broadening, causing P1 to be buried in the shoulder of P2.

To unravel the coupling effect of an array, we next simulated arrays of various sizes. As shown in Figure 5b, P1 gradually re-emerges as the array size was increased from a single disk to a 10 × 10 array (i.e., 100 disks). Interestingly, only 2 disks were needed to cause P1 to reemerge from the shoulder of P2. As the array size increased, P1 gradually shifted toward the higher energy side. The array effect has been explained by FFPC in a similar scenario with gold nanodisk arrays, where blue shift was observed in P2 as the array size increased.[11] As mentioned previously, P1 has not been observed in gold nanodisks even in the high-density array form due to interband damping.[11]

It is important to note that the thickness of the nanodisks plays an important role for array coupling. Our simulation

DOI: 10.1021/acsami.8b17876
ACS Appl. Mater. Interfaces 2019, 11, 2273−2281

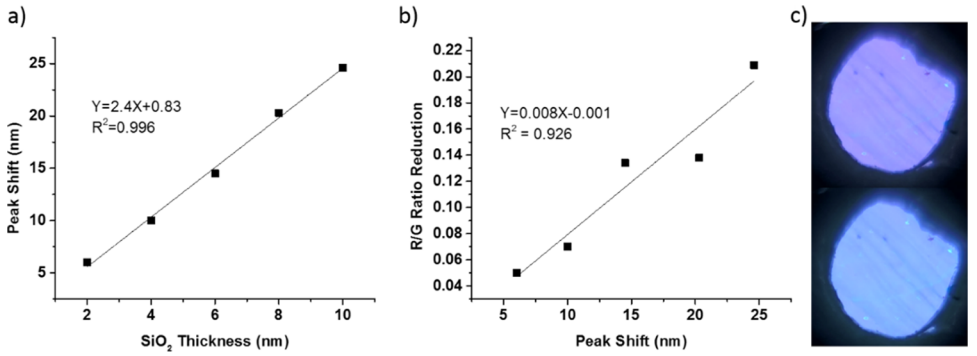

Figure 7. (a) P1 shifts induced by different coating thicknesses of the SiO_2 layer. The sensitivity is roughly 2.4 nm per nanometer of SiO_2. (b) R/G ratio reduction of the smartphone images with different peak shift. The reduction shows a linear trend with the peak shift, as predicted by the simulation provided in the Supporting Information. (c) Smartphone images of the sample before and after coating of 10 nm of SiO_2.

results indicated that P1 was not observed from ANA with disk thickness of 20 nm and started to emerge when the thickness was about 40 nm. As the disk thickness increases, its scattering strength increases and thus leads to the FFPC effect. This is consistent with our previous observation in far-field coupled Au disk array.[11]

As discussed previously, the E-field distributions of the two hybridized modes are distinct, which suggests the possibility of independently tuning P1 and P2 by adjusting RIs of the superstrate and substrate, respectively. As shown in Figure 6a, when the substrate is changed to indium tin oxide (ITO), a higher RI material, P2 red-shifts more significantly compared to P1. A broader P1 is observed on ITO compared to glass, which is likely due to the waveguide mode induced by the ITO layer and its interaction with the LSPR.[43]

While P2 can be preferentially tuned by adjusting the substrate material, P1 is more sensitive to the superstrate. Figure 6b shows the extinction spectra of the ANA fabricated on ITO immersed in solutions of various RIs. The peak positions of P1 are read out and plotted against the surrounding RI in Figure 6c. The sensitivity of P1 is calculated to be 344 nm/RIU with a figure-of-merit ~3. As shown in Figure 6d, the index sensitivity of P1 is higher than three representative classes of substrate-bound plasmonic nanostructures with similar resonance peak positions.[22,44−50] First, for individual Au and Ag nanoparticles of various shapes, RI sensitivity typically increases when the LSPR peak wavelength is redder in air. Au nanoparticles cannot sustain LSPR peaks below ~550 nm because of the interband transition. Ag nanoparticles have higher sensitivity in the 500−550 nm spectral region. The substrate-bound Ag nanocube reported by Sherry had two peaks at 430 and 510 nm with sensitivities 118 and 146 nm/RIU, respectively.[47] Second, substrate-bound nanoparticle arrays in Figure 6d also have higher sensitivities in the redder region. The silver nanotriangular arrays have LSPR peak ~550 nm with sensitivity about 191 nm/RIU.[51] Au nanodisk array fabricated with nanoimprint lithography has a peak ~840 nm with a sensitivity of 327 nm/RIU. The elliptically shaped nanodisks had another bluer peak at ~630 nm because of the nonsymmetric axes, and its LSPR sensitivity was 197 nm/RIU.[48]

Third, for EOT on metallic films perforated by nanohole arrays, the high sensitivity mode is typically redder than 650 nm. Although a 540 nm peak can be obtained from a double nanohole array, its sensitivity suffers from the interband transition of gold.,[46] Overall, our ANA provides the highest RI sensitivity in the green compared to all existing plasmonic nanostructures, a distinct advantage for RGB colorimetric sensing.

Sub-Monolayer Protein Binding Detection by Smartphone Colorimetry. Next, we examine the utility of P1 for biosensing by RGB colorimetry using a smartphone camera as an example. All results below were obtained from ANA on ITO-coated glass substrates. Without losing generality, we employed a well-known protein−protein interaction of biotin and streptavidin. We expect that the framework established here can be translated to various surface binding assays utilizing DNA and/or aptamer probes and antibodies.

We first describe the basic sensing principle. Starting with P1 at ~540 nm in air, increasing RI due to surface coating or binding will cause P1 to red-shift. Imaged by a RGB camera, the red/green ratio (R/G ratio) can be used for quantifying red shifts. We expect that the red-shifted P1 will diminish the R intensity while the G intensity increases, leading to a decreasing R/G ratio. The ratiometric technique is self-referencing, which makes it much more reliable than using absolute intensity values. To determine the optimal P1 wavelength for such an experiment, a simple simulation has been carried out as described in Figure 1 in the Supporting Information. According to this simplified simulation, P1 needs to be redder than 530 nm, which is roughly the center wavelength of the green region, so that a monotonically decreasing R/G ratio can be guaranteed. This simulation also indicates that such a monotonic trend can be continued for over 50 nm of red shift.

By using 480 nm PS beads, P1 was tuned to ~540 nm by fabricating the ANA on ITO. As discussed previously, using the ITO substrate caused much greater red-shift in P2 than P1, allowing the two peaks to become farther apart as shown in Figure 6a.

To calibrate the R/G ratio technique, the samples were first coated with different thicknesses of SiO_2 by electron beam evaporation. The extinction spectra and smartphone images were acquired before and after the SiO_2 deposition. The setup used for taking smartphone images is provided in Figure S2. Such configuration ensured the same area of the sample was measured. Figure 7a shows the amount of P1 shift vs. SiO_2 thickness, which bears a linear relationship with an R^2 value of 0.996. P1 red-shifts about 2.4 nm with 1 nm of SiO_2. The reduction of R/G ratio was calculated from the smartphone images and plotted against the peak shift in Figure 7b. A linear relationship is observed with an R^2 value of 0.926. Worth

DOI: 10.1021/acsami.8b17876
ACS Appl. Mater. Interfaces 2019, 11, 2273−2281

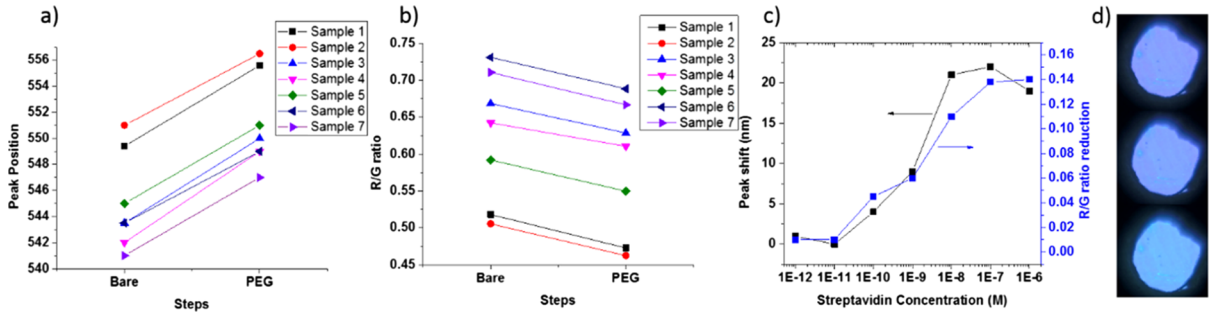

Figure 8. (a) P1 position before and after the modification of the thiol-PEG-biotin SAM. (b) R/G ratio of samples before and after the modification. (c) Peak shifts (black) and R/G ratio reduction (blue) induced by incubation in streptavidin solutions with different concentrations. (d) Smartphone images of the bare sample (top), sample modified with thiol-PEG-biotin (middle), and sample incubated with 10^{-6} M of streptavidin (bottom).

mentioning here is that due to the slight difference in the P1 locations and shapes, different samples have different initial R/G ratios. Even so, the linearity in Figure 7b shows that the reduction of the R/G ratio induced by the peak shift is consistent across different samples. The color change is also visible to the naked eyes with a red shift larger than ~10 nm. The smartphone images of the sample before and after the coating of 10 nm SiO_2 are shown in Figure 7c. The image after the coating has a cooler color tone, which corresponds to the decrease of warm color (yellow and red) and the increase of cool color (green).

The same setup was used for detecting surface binding of biological molecules. In this experiment, the conjugation of streptavidin to surface-bound biotin-poly(ethylene glycol) (PEG)-thiol self-assembled monolayer (SAM) was used as an example. P1 position and the R/G ratio before and after the biotin-PEG-thiol modification are plotted in Figure 8a,b, respectively. On average, the PEG layer caused P1 to red-shift for 6.1 nm with a standard deviation of 0.54 nm. The peak shifts induced an R/G ratio reduction of 0.041 with a standard deviation of 0.004. These sets of data further demonstrate uniform R/G ratio reduction after the same modification even though the initial R/G ratios across samples were different (Figure 8b).

The amounts of P1 shift and the R/G ratio reduction induced by the conjugation of streptavidin molecules with various concentrations are plotted in Figure 8c. The black curve is the peak shift and the blue curve is the reduction in R/G ratio. With concentrations higher than 10^{-10} M, P1 had measurable peak shift which increased with increasing concentration. The peak shift saturated at around 20 nm with 10^{-8} M or higher concentrations. The reduction in the R/G ratio corresponds well with the shift, showing a similar trend, and the maximum reduction of the R/G ratio induced by streptavidin was about 0.14. The corresponding smartphone images of the sample after various steps are provided in Figure 8d. From the top to the bottom are the images of the bare sample, thiol-PEG-biotin-modified sample, and streptavidin-conjugated sample, respectively. The color change is not obvious to the naked eyes with the modification of PEG. However, it is clearly revealed by the R/G ratio. This shows the performance of our analysis in detecting subtle color changes. Furthermore, the plateauing observed in Figure 8c suggests that the sensor can detect sub-monolayer of streptavidin−biotin conjugation.

The color change induced by streptavidin is much more prominent, leading to the detection of SAM of proteins by the naked eyes. The streptavidin modifications were also carried out on selected areas on a single ANA sample. As shown in Figure 9, on a PEG-modified sample (a), 2 μL of deionized

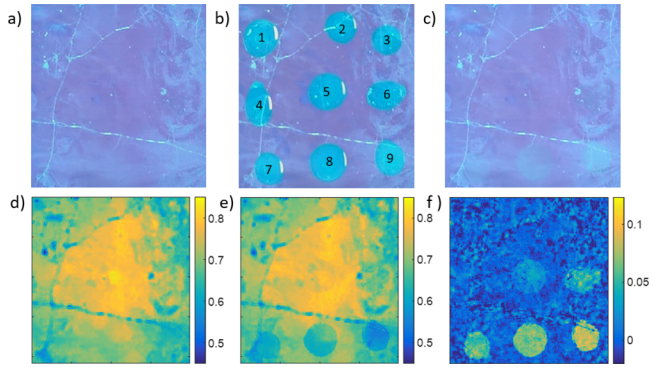

Figure 9. Streptavidin conjugation of selected areas on a single ANA sample. (a) Thiol-PEG-biotin-modified sample, the sample area is roughly 5 mm × 5 mm. (b) 2μL of DI water (1) and streptavidin solutions with concentration ranging from 10^{-13} to 10^{-6} M (2−9) pipetted on the sample. (c) Streptavidin-conjugated sample. (d) R/G ratio map calculated from (a). (e) R/G ratio map calculated from (c). (f) R/G ratio reduction map calculated by subtracting (e) from (d).

(DI) water (1) and streptavidin solutions with concentration ranging from 10^{-13} to 10^{-6} M (2−9) were pipetted onto the sample (b). The sample was then kept in a humidity controlled chamber to prevent the solvent from drying. Because of water-induced large red shift, the droplet-covered sample area appears to be blue-greenish in color. After the incubation, the sample was thoroughly washed with DI water and dried by nitrogen flow as shown in (c). The R/G ratio map of the thiol-PEG-biotin modified sample (d) and streptavidin conjugated sample (e) were calculated from (a,c). By subtracting (e) from (d), the R/G ratio reduction map (f) was obtained. The results correspond well with the previous conclusion, where the lowest detectable concentration was 10^{-10} M.

It is difficult to compare sensor sensing capability (i.e., lowest detection limit) when different proteins are used as targeting molecules because of the up to 7 orders of magnitude difference in the binding affinity.[36] However, by comparing with similar works, the performance of the sensor can be assessed. Cetin, Coskun, and co-workers reported a state-of-the-art work,[28] where a portable device can detect a 3 nm protein layer. In our work, the protein layer is also estimated to be 2−3 nm in thickness, demonstrating a similar level of

DOI: 10.1021/acsami.8b17876
ACS Appl. Mater. Interfaces 2019, 11, 2273−2281

sensitivity. However, in our study, the requirement for the plasmonic substrate is much less restrictive, and therefore a large-scale, low-cost fabrication method can be used. Furthermore, the utilization of the smartphone camera eliminated the need for an additional charge-coupled device (CCD) camera, reducing the cost for the portable device. Finally, a broadband white light source was used as light source in the experiment, further simplifying the design. In principle, even the sun light can be a viable source.

CONCLUSIONS

In conclusion, we have discovered that the silver-rich Au−Ag alloy nanodisk supports a prominent high energy resonance located around 540 nm, the most sensitive region for a RGB camera. The origin of this high energy resonance stems from symmetry-breaking when the arrays are placed in between a substrate and a superstrate. This strategy has never been realized for two reasons: first, although such mode splitting has been known for Ag nanoparticles, the silver material has poor environmental stability and thus hindered its practical use. Second, the high energy resonance mode is heavily dampened in Au due to interband transition. In this paper, we have shown that the high energy mode can be partially restored for silver-rich alloy nanodisk, which has excellent environmental stability. However, peak broadening occurs due to plasmonic dephasing when the nanodisk diameter increases, which is necessary to precisely place it near 540 nm. We have next demonstrated that a far-field coupled alloy nanodisk array (ANA) fabricated by low-cost NSL can fully restore the high energy mode with electric field concentration extended into the superstrate, thereby imparting greater sensitivity to local RI changes. The high energy mode at 540 nm is of key importance for color change detection using low cost RGB cameras and extended light sources. As most RI-sensitive plasmonic nanostructures rely on resonances in the red or NIR portions of the spectrum, they are incompatible with RGB cameras commonly found in consumer electronics such as smartphones, webcams, tablets, and so on. The reason for this is when the original resonance is already in the red or NIR region, further red shift due to surface binding cannot be quantified by a RGB sensor. Instead, a spectrum needs to be taken, which requires additional components such as a spectrometer, scientific camera, and highly stable, monochromatic light source. The index sensitivity of ANA is the highest among known plasmonic resonance (particles or holes) within a similar wavelength region. We demonstrate colorimetric detection (ratio of R/G) of sub-nanomolar and sub-monolayer biotin-streptavidin surface binding with a smartphone camera and a white light lamp. The high performance yet low-cost fabrication and detection technology could potentially result in affordable point-of-care biosensing technologies. Because the color change is visible by naked eyes and can be detected by RGB colorimetry, the ANA substrate and the sensing scheme have great potential in point-of-care diagnostics under resource-limited condition due to the low-cost, high-yield fabrication process, no need of a separate CCD camera and the fact almost any broadband light source can be used.

MATERIAL AND METHODS

Material. Chloroform (anhydrous, ≥99.0%), thiol-PEG-biotin, streptavidin, and latex beads (PS beads, 10% aqueous suspension) with mean particle sizes 460/480/600/800 nm were purchased from Sigma-Aldrich. Ethanol (200 proof) was from Decon Laboratories, Inc. Silicon wafers (p-type) were obtained from University Wafers and coverslips (22 × 40 mm, No. 1) from VWR. Gold and silver sputtering targets (>99.99%) were purchased from ACI Alloys, Inc. Oxygen gas (99.99%) and argon gas (99.999%) was used for reactive ion etching and ion milling, respectively.

Fabrication Process. The fabrication process was described in detail in our previous works. Briefly, a silver−gold alloy film of prescribed composition and thickness was deposited onto coverslip glass precleaned in ethanol using dual-target cosputtering deposition. A monolayer of PS beads exhibiting polycrystalline structure was then assembled on the metal layer. The PS beads were then shrunk to the desired diameter in O_2 plasma, followed by Ar^+ ion milling to transfer the bead pattern into the metal film. The remaining PS beads were then removed by sonication in chloroform.

Sample Characterization. The extinction spectrum measurements were carried out using a Cary 5000 spectrophotometer by measuring the optical transmission in the forward direction. The spectral peak position was determined by locating the resonance maximum. For detection of the surface modification, the color of the samples before and after modification was analyzed by taking cell phone images. The schematic setup for such measurement is shown in Supporting Information Figure S2.

FDTD Simulation. The FDTD simulation setup was described in detail in our previous works and briefly outlined here.[11] For a polycrystalline array, the centroids of an ANA from a typical SEM image containing 115 particles are read out and their relative locations are used as the array arrangement used in the FDTD simulations. The ANAs used in the FDTD simulation are generated first by scaling the centroid position to the desired center-to-center distance, and then 3D alloy disk structures with predetermined thickness and diameters are added to all the centroid positions. For periodic arrays, the 100 centroids (10 by 10) are generated with the desired periodicity with hexagonal packing and 3D alloy disk structures are added to each of the centroid positions. In the simulation, alloy disks are located on a glass substrate with a RI of 1.52. The total field scattered field (TFSF) light source was used in the simulation for collecting the scattering and absorption cross-sections. Both for single particle and large array simulations, the number of perfectly matched layers was set to 12. The boundaries of simulations were separated from TFSF source by at least 1 microns, so that reflection from the PML layers does not interfere in the convergence of the simulations. For single disks, the effect of staircase approximation was addressed by reducing the mesh size around the disk to 2 nm × 2 nm × 2 nm. For large array simulations, the mesh size was 8 nm × 8 nm × 8 nm. The simulation time step (dt) had the default value of 0.99. An air gap with various specified separations was provided between the particle array and the glass substrate to simulate the extinction for particles at that particular distance from the substrate. For the substrate at infinite distance condition, the simulations were carried out without any substrate in the simulation region. The dielectric constant of the alloy is calculated with an analytical model provided in the literature.[42]

SAM Modification. To prevent the silver content interfering with the sulfur−gold bonding, the samples are coated with an additional 2 nm of gold by sputtering deposition. The additional coating of gold did not have a significant impact on the extinction spectra of the samples. The samples are first immersed in 200 proof ethanol for 24 hours before surface modification. Then, the bare samples are incubated in 1 mM PEG solution for 24 h, followed by extensive rinsing with DI water and drying by nitrogen gas. Finally, the PEG-modified samples are further modified with streptavidin solution in two schemes. In the first scheme, the samples were incubated in streptavidin solutions with concentrations ranging from 10^{-12} to 10^{-6} M for 2 h. In the second scheme, 2 μL of DI water and streptavidin solutions with concentrations ranging from 10^{-13} to 10^{-6} M was dropped onto one PEG-modified ANA sample. During incubation, the samples were kept in a humidity-controlled container to prevent evaporation of the solution. After incubation, the samples were rinsed with DI water and dried by nitrogen gas flow. At the end of each step

DOI: 10.1021/acsami.8b17876
ACS Appl. Mater. Interfaces 2019, 11, 2273−2281

(including bare samples), the extinction spectra and smartphone images are acquired and analyzed.

■ ASSOCIATED CONTENT

Supporting Information

The Supporting Information is available free of charge on the ACS Publications website at DOI: 10.1021/acsami.8b17876.

Simplified color characterization simulation; color characterization setup; and cross-section schematic for simulations (PDF)

■ AUTHOR INFORMATION

Corresponding Author

*E-mail: wshih@central.uh.edu.

ORCID

Wei-Chuan Shih: 0000-0002-7530-7352

Author Contributions

The manuscript was written through contributions of all authors. All authors have given approval to the final version of the manuscript.

Notes

The authors declare no competing financial interest.

■ ACKNOWLEDGMENTS

W.-C.S. acknowledges the National Science Foundation (NSF) CAREER Award CBET-1151154, NSF CBET-1605683, NSF CBET-1643391.

■ REFERENCES

(1) Hutter, E.; Fendler, J. H. Exploitation of Localized Surface Plasmon Resonance. *Adv. Mater.* **2004**, *16*, 1685−1706.

(2) Willets, K. A.; Van Duyne, R. P. Localized Surface Plasmon Resonance Spectroscopy and Sensing. *Annu. Rev. Phys. Chem.* **2007**, *58*, 267−297.

(3) Anker, J. N.; Hall, W. P.; Lyandres, O.; Shah, N. C.; Zhao, J.; Van Duyne, R. P. Biosensing with Plasmonic Nanosensors. *Nat. Mater.* **2008**, *7*, 442−453.

(4) Willets, K. A.; Wilson, A. J.; Sundaresan, V.; Joshi, P. B. Super-resolution imaging and plasmonics. *Chem. Rev.* **2017**, *117*, 7538−7582.

(5) Atwater, H. A.; Polman, A. Plasmonics for Improved Photovoltaic Devices. *Nat. Mater.* **2010**, *9*, 205−213.

(6) Huang, X.; Tang, S.; Mu, X.; Dai, Y.; Chen, G.; Zhou, Z.; Ruan, F.; Yang, Z.; Zheng, N. Freestanding Palladium Nanosheets with Plasmonic and Catalytic properties. *Nat. Nanotechnol.* **2010**, *6*, 28−32.

(7) Wang, H.; Kundu, J.; Halas, N. J. Plasmonic Nanoshell Arrays Combine Surface-Enhanced Vibrational Spectroscopies on a Single Substrate. *Angew. Chem., Int. Ed.* **2007**, *46*, 9040−9044.

(8) Zhao, F.; Zeng, J.; Parvez Arnob, M. M.; Sun, P.; Qi, J.; Motwani, P.; Gheewala, M.; Li, C.-H.; Paterson, A.; Strych, U.; Raja, B.; Willson, R. C.; Wolfe, J. C.; Lee, T. R.; Shih, W.-C. Monolithic NPG Nanoparticles with Large Surface Area, Tunable Plasmonics, and High-Density Internal Hot-spots. *Nanoscale* **2014**, *6*, 8199−8207.

(9) Chau, Y.-F. C.; Wang, C.-K.; Shen, L.; Lim, C. M.; Chiang, H.-P.; Chao, C.-T. C.; Huang, H. J.; Lin, C.-T.; Kumara, N. T. R. N.; Voo, N. Y. Simultaneous Realization of High Sensing Sensitivity and Tunability in Plasmonic Nanostructures Arrays. *Sci. Rep.* **2017**, *7*, 16817.

(10) Haynes, C. L.; McFarland, A. D.; Zhao, L.; Van Duyne, R. P.; Schatz, G. C.; Gunnarsson, L.; Prikulis, J.; Kasemo, B.; Käll, M. Nanoparticle Optics: The Importance of Radiative Dipole Coupling in Two-Dimensional Nanoparticle Arrays. *J. Phys. Chem. B* **2003**, *107*, 7337−7342.

(11) Zhao, F.; Arnob, M. M. P.; Zenasni, O.; Li, J.; Shih, W.-C. Far-field Plasmonic Coupling in 2-Dimensional Polycrystalline Plasmonic Arrays Enables Wide Tunability with Low-cost Nanofabrication. *Nanoscale Horiz.* **2017**, *2*, 267−276.

(12) Auguié, B.; Barnes, W. L. Collective Resonances in Gold Nanoparticle Arrays. *Phys. Rev. Lett.* **2008**, *101*, 143902.

(13) Prodan, E.; Radloff, C.; Halas, N. J.; Nordlander, P. A Hybridization Model for the Plasmon Response of Complex Nanostructures. *Science* **2003**, *302*, 419−422.

(14) Nordlander, P.; Oubre, C.; Prodan, E.; Li, K.; Stockman, M. I. Plasmon Hybridization in Nanoparticle Dimers. *Nano Lett.* **2004**, *4*, 899−903.

(15) Prodan, E.; Nordlander, P. Plasmon Hybridization in Spherical Nanoparticles. *J. Chem. Phys.* **2004**, *120*, 5444−5454.

(16) Vogel, N.; Fischer, J.; Mohammadi, R.; Retsch, M.; Butt, H.-J.; Landfester, K.; Weiss, C. K.; Kreiter, M. Plasmon Hybridization in Stacked Double Crescents Arrays Fabricated by Colloidal Lithography. *Nano Lett.* **2011**, *11*, 446−454.

(17) Nordlander, P.; Prodan, E. Plasmon Hybridization in Nanoparticles Near Metallic Surfaces. *Nano Lett.* **2004**, *4*, 2209−2213.

(18) Knight, M. W.; Wu, Y.; Lassiter, J. B.; Nordlander, P.; Halas, N. J. Substrates Matter: Influence of an Adjacent Dielectric on an Individual Plasmonic Nanoparticle. *Nano Lett.* **2009**, *9*, 2188−2192.

(19) Sherry, L. J.; Chang, S.-H.; Schatz, G. C.; Van Duyne, R. P.; Wiley, B. J.; Xia, Y. Localized Surface Plasmon Resonance Spectroscopy of Single Silver Nanocubes. *Nano Lett.* **2005**, *5*, 2034−2038.

(20) Ringe, E.; McMahon, J. M.; Sohn, K.; Cobley, C.; Xia, Y.; Huang, J.; Schatz, G. C.; Marks, L. D.; Van Duyne, R. P. Unraveling the Effects of Size, Composition, and Substrate on the Localized Surface Plasmon Resonance Frequencies of Gold and Silver Nanocubes: a Systematic Single-Particle Approach. *J. Phys. Chem. C* **2010**, *114*, 12511−12516.

(21) Zhang, S.; Bao, K.; Halas, N. J.; Xu, H.; Nordlander, P. Substrate-Induced Fano Resonances of a Plasmonic Nanocube: a Route to Increased-Sensitivity Localized Surface Plasmon Resonance Sensors Revealed. *Nano Lett.* **2011**, *11*, 1657−1663.

(22) Chen, H.; Kou, X.; Yang, Z.; Ni, W.; Wang, J. Shape- and Size-Dependent Refractive Index Sensitivity of Gold Nanoparticles. *Langmuir* **2008**, *24*, 5233−5237.

(23) Zhao, W.; Ali, M. M.; Aguirre, S. D.; Brook, M. A.; Li, Y. Paper-Based Bioassays using Gold Nanoparticle Colorimetric Probes. *Anal. Chem.* **2008**, *80*, 8431−8437.

(24) Liu, J.; Lu, Y. A Colorimetric Lead Biosensor using DNAzyme-Directed Assembly of Gold Nanoparticles. *J. Am. Chem. Soc.* **2003**, *125*, 6642−6643.

(25) Larsson, E. M.; Alegret, J.; Käll, M.; Sutherland, D. S. Sensing Characteristics of NIR Localized Surface Plasmon Resonances in Gold Nanorings for Application as Ultrasensitive Biosensors. *Nano Lett.* **2007**, *7*, 1256−1263.

(26) Haes, A. J.; Van Duyne, R. P. A Nanoscale Optical Biosensor: Sensitivity and Selectivity of an Approach Based on the Localized Surface Plasmon Resonance Spectroscopy of Triangular Silver Nanoparticles. *J. Am. Chem. Soc.* **2002**, *124*, 10596−10604.

(27) Kumara, N. T. R. N.; Chau, Y.-F. C.; Huang, J.-W.; Huang, H. J.; Lin, C.-T.; Chiang, H.-P. Plasmonic Spectrum on 1D and 2D Periodic Arrays of Rod-Shape Metal Nanoparticle Pairs with Different Core Patterns for Biosensor and Solar Cell Applications. *J. Opt.* **2016**, *18*, 115003.

(28) Cetin, A. E.; Coskun, A. F.; Galarreta, B. C.; Huang, M.; Herman, D.; Ozcan, A.; Altug, H. Handheld High-Throughput Plasmonic Biosensor using Computational on-chip Imaging. *Light: Sci. Appl.* **2014**, *3*, e122.

(29) Zeng, S.; Yong, K.-T.; Roy, I.; Dinh, X.-Q.; Yu, X.; Luan, F. A Review on Functionalized Gold Nanoparticles for Biosensing Applications. *Plasmonics* **2011**, *6*, 491−506.

(30) Dutta, S.; Saikia, K.; Nath, P. Smartphone Based LSPR Sensing Platform for Bio-conjugation Detection and Quantification. *RSC Adv.* **2016**, *6*, 21871−21880.

(31) Tang, L.; Li, J. Plasmon-Based Colorimetric Nanosensors for Ultrasensitive Molecular Diagnostics. *ACS Sens.* **2017**, *2*, 857−875.
(32) Zhu, H.; Isikman, S. O.; Mudanyali, O.; Greenbaum, A.; Ozcan, A. Optical Imaging Techniques for Point-of-Care Diagnostics. *Lab Chip* **2013**, *13*, 51−67.
(33) Haes, A. J.; Chang, L.; Klein, W. L.; Van Duyne, R. P. Detection of a Biomarker for Alzheimer's Disease from Synthetic and Clinical Samples using a Nanoscale Optical Biosensor. *J. Am. Chem. Soc.* **2005**, *127*, 2264−2271.
(34) Drain, P. K.; Hyle, E. P.; Noubary, F.; Freedberg, K. A.; Wilson, D.; Bishai, W. R.; Rodriguez, W.; Bassett, I. V. Diagnostic Point-of-Care Tests in Resource-Limited Settings. *Lancet Infect. Dis.* **2014**, *14*, 239−249.
(35) Zhang, D.; Liu, Q. Biosensors and bioelectronics on smartphone for portable biochemical detection. *Biosens. Bioelectron.* **2016**, *75*, 273−284.
(36) Zhang, S.; Garcia-D'Angeli, A.; Brennan, J. P.; Huo, Q. Predicting Detection Limits of Enzyme-Linked Immunosorbent Assay (ELISA) and Bioanalytical Techniques in General. *Analyst* **2014**, *139*, 439−445.
(37) Nguyen, H.; Sung, Y.; O'Shaughnessy, K.; Shan, X.; Shih, W.-C. Smartphone Nanocolorimetry for On-Demand Lead Detection and Quantitation in Drinking Water. *Anal. Chem.* **2018**, *90*, 11517−11522.
(38) Sung, Y.-L.; Jeang, J.; Lee, C.-H.; Shih, W.-C. Fabricating optical lenses by inkjet printing and heat-assistedin situcuring of polydimethylsiloxane for smartphone microscopy. *J. Biomed. Opt.* **2015**, *20*, 047005.
(39) Lee, S.; Kim, G.; Moon, J. Performance Improvement of the One-Dot Lateral Flow Immunoassay for Aflatoxin B1 by using a Smartphone-Based Reading System. *Sensors* **2013**, *13*, 5109−5116.
(40) Zangheri, M.; Cevenini, L.; Anfossi, L.; Baggiani, C.; Simoni, P.; Di Nardo, F.; Roda, A. A Simple and Compact Smartphone Accessory for Quantitative Chemiluminescence-Based Lateral Flow Immunoassay for Salivary Cortisol Detection. *Biosens. Bioelectron.* **2015**, *64*, 63−68.
(41) Doeven, E. H.; Barbante, G. J.; Harsant, A. J.; Donnelly, P. S.; Connell, T. U.; Hogan, C. F.; Francis, P. S. Mobile phone-based electrochemiluminescence sensing exploiting the 'USB On-The-Go' protocol. *Sens. Actuators, B* **2015**, *216*, 608−613.
(42) Rioux, D.; Vallières, S.; Besner, S.; Muñoz, P.; Mazur, E.; Meunier, M. An Analytic Model for the Dielectric Function of Au, Ag, and their Alloys. *Adv. Opt. Mater.* **2013**, *2*, 176−182.
(43) Linden, S.; Kuhl, J.; Giessen, H. Controlling the Interaction between Light and Gold Nanoparticles: Selective Suppression of Extinction. *Phys. Rev. Lett.* **2001**, *86*, 4688.
(44) Martinsson, E.; Otte, M. A.; Shahjamali, M. M.; Sepulveda, B.; Aili, D. Substrate Effect on the Refractive Index Sensitivity of Silver Nanoparticles. *J. Phys. Chem. C* **2014**, *118*, 24680−24687.
(45) Im, H.; Sutherland, J. N.; Maynard, J. A.; Oh, S.-H. Nanohole-based Surface Plasmon Resonance Instruments with Improved Spectral Resolution Quantify a Broad Range of Antibody-Ligand Binding Kinetics. *Anal. Chem.* **2012**, *84*, 1941−1947.
(46) Lesuffleur, A.; Im, H.; Lindquist, N. C.; Oh, S.-H. Periodic Nanohole Arrays with Shape-Enhanced Plasmon Resonance as Real-time Biosensors. *Appl. Phys. Lett.* **2007**, *90*, 243110.
(47) Mayer, K. M.; Hafner, J. H. Localized Surface Plasmon Resonance Sensors. *Chem. Rev.* **2011**, *111*, 3828−3857.
(48) Lee, S.-W.; Lee, K.-S.; Ahn, J.; Lee, J.-J.; Kim, M.-G.; Shin, Y.-B. Highly Sensitive Biosensing using Arrays of Plasmonic Au Nanodisks realized by Nanoimprint Lithography. *ACS Nano* **2011**, *5*, 897−904.
(49) Lee, Y. H.; Chen, H.; Xu, Q.-H.; Wang, J. Refractive Index Sensitivities of Noble Metal Nanocrystals: The Effects of Multipolar Plasmon Resonances and the Metal Type. *J. Phys. Chem. C* **2011**, *115*, 7997−8004.
(50) Offermans, P.; Schaafsma, M. C.; Rodriguez, S. R. K.; Zhang, Y.; Crego-Calama, M.; Brongersma, S. H.; Gómez Rivas, J. Universal Scaling of the Figure of Merit of Plasmonic Sensors. *ACS Nano* **2011**, *5*, 5151−5157.
(51) Malinsky, M. D.; Kelly, K. L.; Schatz, G. C.; Van Duyne, R. P. Chain Length Dependence and Sensing Capabilities of the Localized Surface Plasmon Resonance of Silver Nanoparticles Chemically Modified with Alkanethiol Self-assembled Monolayers. *J. Am. Chem. Soc.* **2001**, *123*, 1471−1482.

DOI: 10.1021/acsami.8b17876
ACS Appl. Mater. Interfaces 2019, 11, 2273−2281